

# **Pyramidal dislocation driven martensitic nucleation: A step toward consilience of deformation scenario in fcc materials (II)**

Tae-Ho LEE <sup>1,\*</sup>, Heon-Young HA <sup>1</sup>, Seong-Hoon KIM <sup>1</sup>, Hyung-Kwon PARK <sup>1</sup>

Seong-Jun PARK <sup>1</sup>, Chang-Hoon LEE <sup>1</sup>, Subin LEE <sup>2,\*</sup> and Christoph Kirchlechner <sup>2,\*</sup>

1 *Extreme Materials Research Institute, Korea Institute of Materials Science, 797  
Changwondaero, Changwon 51508, Republic of Korea*

2 *Institute for Applied Materials, Karlsruhe Institute of Technology, Kaiserstrasse 12, Karlsruhe  
76131, Germany*

---

\* Corresponding authors:

Tae-Ho LEE (E-mail: [lth@kims.re.kr](mailto:lth@kims.re.kr))

Tel.: +82-55-280-3434 / Fax.: +82-55-280-3599

Subin LEE (E-mail: [subin.lee@kit.edu](mailto:subin.lee@kit.edu) )

Christoph Kirchlechner (E-mail: [Christoph.kirchlechner@kit.edu](mailto:Christoph.kirchlechner@kit.edu))



## **Abstract**

Dislocation glides and their interactions with other defects are central to our understanding of deformation mechanism enhancing plasticity and damage tolerance. Martensitic transformation (MT) is a fascinating phenomenon overcoming strength-elongation trade-off and thus tailoring structure-property architecture. However, dislocation plasticity of Fe-based hexagonal close-packed (hcp) martensite is still challenging due to its metastability, further complicated by controversies surrounding pyramidal dislocation even in pure hcp metals. To resolve the uncertainties, we address the pyramidal-dislocation-driven plasticity in Fe-based hcp martensite by employing in-situ transmission electron microscopy (TEM) and high-resolution (HR) annular bright field (ABF) imaging together with dislocation-contrast analyses. We show that the activation and dissociation of pyramidal dislocation govern the initial stage of plastic deformation, while subsequent cross-slip by the cooperative motion of dissociated pyramidal dislocations plays a key role in nucleation of new hcp martensite. By incorporating current dislocation model into previous models coupled with stacking-fault-energy concept, we propose a synthesized deformation scenario that offers a comprehensive perspective on plasticity and transformability.

**Keywords:** Martensitic transformation; pyramidal dislocation; deformation; TEM

## 1. Introduction

Dislocations are the essential carriers of plastic flow during crystal deformation, and their interactions with various defects ranging from other dislocations (1D), grain boundaries (2D) to precipitates (3D) are central to our understanding of deformation mechanisms guaranteeing superior plasticity and enhanced damage tolerance [1-5]. Among various types of deformation mechanisms, martensitic transformation (MT) has been a subject of practical and theoretical importance [6-9], especially, in austenitic steels with face-centered cubic (fcc) structure, owing to its essential role in plasticity (TRIP: TRansformation-Induced Plasticity) [7, 9, 10] and thermo-elasticity, known as shape memory effect (SME) [11, 12]. A fundamental understanding of MT together with finely-resolved knowledge of dislocation reaction is crucial for tailoring the microstructure-property relationship as well as for optimizing the composition-processing parameters in development of high-performance MT-based materials. Although dislocation models elucidating nucleation of body-centered cubic (bcc) martensite have been well established [6-10], dislocation model governing plasticity of hcp martensite itself is still challenging because of the following reasons.

First, due to its metastability nucleating in the intermediate stage of phase transformation (fcc  hcp  bcc), most of previous models have interpreted dislocation reactions in the view of fcc matrix [7, 10, 13], rather than hcp martensite per se. Although fcc matrix and hcp martensite are close-packed structure and keep well-known Shoji-Nishiyama orientation relationship (OR) [6] wherein the close-packed planes and directions of both structures are parallel, there are significant differences in the dislocation plasticity of two phases. Compared to fcc structure, whose primary slip system includes twelve equivalent systems, the lower

crystalline symmetry of hcp structure results in a reduced number of equivalent primary slips and anisotropy in plasticity [3, 14]. To visualize more complete picture highlighting deformation mechanisms, further insight should be gleaned from examining the dislocation reaction governing the intermediate stage of MT.

Second, the low ductility of hcp-based materials at room temperature has been a major obstacle hampering their widespread applications [1, 3, 14]. To overcome the problem, the strategies have been aimed at energetically enhancing the ability to accommodate the strain along c-axis, which can be more effectively accomplished by  $\langle c+a \rangle$  pyramidal slip than by deformation twinning [14-16]. However, controversy remains as to the intrinsic nature of pyramidal dislocations, even in pure hcp metals, such as their ability to accommodate plastic strain and slip pathways including major slip plane and possibility or route of cross slip [3, 15-17]. The disagreements regarding the pyramidal-dislocation-driven plasticity certainly point to the need for further research unraveling the mystery underlying dislocation activities to be taken into account.

In what follows, by employing in-situ transmission electron microscopy (TEM) and high-resolution (HR) annular bright field (ABF) imaging together with dislocation-contrast analyses, we address the dislocation plasticity of Fe-based hcp martensite to tackle the aforementioned two issues. By standing on the understanding of its general plasticity, we further show pyramidal dislocation plays an indispensable role in strain-induced nucleation of new hcp martensite. Through incorporating our dislocation model into previous models coupled with stacking-fault-energy (SFE) concept that has been regarded as a governing factor for entire deformation mechanism of fcc-based materials [18-20] and on continuation of our previous



investigation [21], we go one step further to propose a consilience of deformation scenario by categorizing into first- and second-order hierarchy driven by dissimilar governing factors (dissociation route of perfect dislocation in fcc matrix for 1<sup>st</sup> order and dislocation plasticity of hcp martensite itself for 2<sup>nd</sup> order hierarchy of deformation mechanism). These results provide fundamental and predictive insight into plasticity and transformability and have substantial implications for utilizing dislocation plasticity to realize a new strategy required for development of higher performance materials.

## **2. Experimental**

The investigated material is an fcc-based austenitic steel whose chemical composition is 18.12Cr; 9.66Mn; 0.22Si; 0.01Mo; 0.38N; 0.15C (all in weight percent). The 10kg ingot was fabricated using a vacuum induction melting furnace (VIM 4 III-P, ALD, Germany). After homogenization at 1,250 °C for two hours in Ar atmosphere, the ingot was hot-rolled into sheet with 4 mm thickness. The specimens were solution-annealed at 1,050 °C for one hour in the fcc austenite ( $\gamma$ ) single-phase region and then quenched into water. Deformation microstructures were characterized by three different transmission electron microscopes (TEM). (1) The dislocation configuration and determination of the Burgers vectors of the dislocations were examined by means of TEM (JEM-2100F, JEOL Ltd, Japan.) equipped with a high-angle tilting stage ( $x = \pm 45^\circ$ ,  $y = \pm 45^\circ$ ). Thin foils for all the TEM observations were prepared in a twin-jet electrolytic polishing apparatus using a solution containing 15% perchloric acid and 85% methanol. The Burgers vectors of dislocations were determined based

on invisibility criteria by judging their visibility or invisibility in bright-field (BF) TEM images under two-beam diffraction conditions. Simulated selected area diffraction (SAD) patterns and the stereographic projections used to navigate orientation space were generated by the software, Desktop Microscopist. (2) Samples for the in-situ tensile TEM experiments were prepared to specific dimensions (3 mm×12 mm) by punching the polished foil using a custom-made foil puncher. The in-situ TEM samples were also finally etched using the aforementioned etching condition. The TEM (JEM 2100, JEOL Ltd, Japan.) equipment was operated at an acceleration voltage of 200 kV, and an in-situ straining TEM holder (straining in situ holder model 654, Gatan, Inc, USA.) was used for the in-situ experiments. (3) Atomic resolution images were recorded with scanning transmission electron microscope (STEM; JEOL JEM-2100F, JEOL Ltd., Tokyo, Japan) equipped with an aberration corrector (CEOS GmbH, Heidelberg, Germany). The probe diameter of the beam was approximately 0.9 Å under an acceleration voltage of 200 kV. The raw ABF (annular bright field) STEM images were filtered to eliminate the background noise (Radial Difference Filters, HREM Research Inc.). For the quantitative analysis of local strain components in the TEM samples, GPA (Geometric phase analysis) technique was used, which allows mapping two-dimensional local displacement fields by analyzing the phase shift between non-collinear Fourier components of the lattice vectors  $g_1$  and  $g_2$ . The GPA analysis was conducted by a commercial software (HREM-Filters Pro, HREM Research Inc.), Matlab software was used to visualize the GPA results.

### **3. Results**

### 3. 1 Whole picture of martensitic transformation (MT)

The entire picture of MT, together with typical true stress ( $\sigma_t$ ) versus true strain ( $\varepsilon_t$ ) curve and the change in volume fractions of constituting phases measured by Rietveld whole-profile fitting using TCH function on neutron diffraction profiles in our previous work [20], during uniaxial tensile deformation are summarized in Fig. 1. To visualize more clear definition, a schematic illustration distinguishing three distinct types of hcp martensites ( $\varepsilon_A$ ,  $\varepsilon_B$  and  $\varepsilon_{New}$ ) is also given in Fig. 2). Upon tensile straining, the  $\sigma_t$  vs  $\varepsilon_t$  curve shows a sigmodal shape at  $\varepsilon_t \sim 20\%$  and the investigated steel shows an excellent strength-elongation balance. At an early stage of deformation, perfect dislocations dissociate into partial dislocations and stacking faults form in between the dissociated partials. The fcc-to-hcp MT (Fig. 1a) represents a fundamental aspect of initial stage of plastic deformation. Here, a Frank partial dislocation, resulting from the dissociation of a screw-type perfect dislocation, plays an important role in nucleation of hcp martensite (designated as  $\varepsilon_A$ ) [21]. Subsequently, two distinct types of MT were identified: the formation of new hcp martensite ( $\varepsilon_{New}$ ) from pre-existing  $\varepsilon_A$ , and the nucleation of bcc ( $\alpha'$ ) martensite at the intersection of two hcp martensites [22] - one being  $\varepsilon_A$ , and the other designated as conjugated hcp martensite ( $\varepsilon_B$ ) glided along different slip system of  $\gamma$  matrix, as indicated in Fig. 2. It is noted that the change in  $\sigma_t$  vs  $\varepsilon_t$  curve into a sigmodal shape is attributed to formation of bcc martensite, which is known as TRIP effect [10].

In summary, the hierarchy of MT is categorized into two orders: (1) The first-order hierarchy (fcc-to-hcp MT), wherein austenite ( $\gamma$ ) matrix initially transforms into hcp martensite

( $\varepsilon_A$ ); (2) The second-order hierarchy, in which, with incremental straining, the product of first-order MT,  $\varepsilon_A$ , subsequently undergoes the next step of MT: (Stage I) autocatalytic formation of new hcp martensite ( $\varepsilon_{New}$ ) from pre-existing  $\varepsilon_A$  (Fig. 1b); (Stage II) hcp-to-bcc MT (Fig. 1c) at the intersection of two hcp martensites ( $\varepsilon_A$  and  $\varepsilon_B$ ). Based on the change in volume fraction of hcp martensite, it is conceivable that the transition from Stage I to Stage II may occur between 20% and 30% of true strain. We found that the transformation route into stage I or II strongly depends on whether the hcp-hcp intersection occurs or not [22]. In the following, we focus on the former (Stage I) whose dislocation model has not been established yet.

### 3. 2 Dislocation motion revealed by in-situ TEM deformation

To directly observe the overall landscape of dislocation activities responsible for the formation of  $\varepsilon_{New}$ , in-situ TEM straining experiments were performed (Fig. 3 and Movie S1). A series of successive frames extracted from in-situ TEM movie shows the nucleation of  $\varepsilon_{New}$  from  $\varepsilon_A$  and consecutive dislocation motion (The important pyramidal slip systems and the crystallographic information of our hcp martensite measured from Rietveld refinement on neutron diffraction profile [20] are given in Fig. 4). At the beginning of deformation, the easy glide of  $\langle a \rangle$  dislocations ( $\vec{b} = \frac{1}{3} \langle 1\bar{1}00 \rangle$ ) having wavy morphology along basal plane is dominant (left side of Fig. 3a). Upon further deformation, pyramidal dislocations (Fig. 3a) oblique to basal planes are activated, and they concurrently interact with the moving  $\langle a \rangle$  dislocations (Fig. 3b). Close interaction of the pyramidal dislocation with  $\langle a \rangle$  dislocation triggers cross-slip (Fig. 3c). Once the cross slip takes place, another component of pyramidal dislocation is also activated with different gliding direction onto another pyramidal plane of

$\varepsilon_{\text{New}}$ . After some dislocations cross-slipped to another slip plane, significant plastic flow occurred on the cross-slipped plane instead of the continuous glide of dislocations. Once the dislocations leave the cross-slipped region, the dislocations move slower and the width of  $\varepsilon_A$  becomes reduced (Fig. 3c), which implies that the formation of  $\varepsilon_{\text{New}}$  effectively contributes to the stress relaxation (accommodation).

### 3. 3 Atomic structural analysis for nucleation of $\varepsilon_{\text{New}}$

To get a better understanding of dislocation activities, we examine the atomic configuration at the onset of  $\varepsilon_{\text{New}}$  nucleation using aberration-corrected ABF-STEM imaging together with stereographic projection (SP) (Figs. 5 and 6). The atomic arrangements in the right side of the figure corresponds to perfect hcp structure ( $\varepsilon_A$ ) and one atomic layer of stacking fault (SF) parallel to close-packed  $(0001)_{\varepsilon_{1st}}$  plane is distinguished (indicated by dotted green arrow), which leads to the change in stacking sequence from ABAB... to AB/CBCB.... On the close inspection of ABF-STEM image, we find that the newly-formed hcp martensites ( $\varepsilon_{\text{New}}$ ) containing a few unit cells are gradually generated by shearing of atomic plane of  $\varepsilon_A$ , and they are related to each other by rotational relationship of  $67^\circ$  (as highlighted in bottom of Fig. 5a). Geometric phase analysis (GPA) to assess the strain fields related to  $\varepsilon_{\text{New}}$  formation is performed (Fig. 5b). It is found that, in the vicinity of dislocation core of  $\varepsilon_{\text{New}}$ , the compressive and tensile strains are generated lying parallel to the diagonal direction of  $\varepsilon_A$  and highly localized in a direction perpendicular to sheared trace ( $\varepsilon_{xy} < 0\bar{1}11 >$ ), confirming the presence of edge-type  $\langle c+a \rangle$  dislocation.

Based on Burgers circuit (Fig. 5c) and trace analysis in SP (Fig. 6), the edge component of

the dislocation is determined to be  $\frac{1}{3} \langle 0\bar{1}11 \rangle$  of  $\varepsilon_A$  (orange-dotted arrow), from which it is concluded that the edge-type pyramidal dislocation in pre-existing  $\varepsilon_A$  plays an important role in the formation of  $\varepsilon_{New}$ . The crystallographic relationships among  $\varepsilon_A$ ,  $\varepsilon_{New}$  (yellow-colored box) and fcc matrix (sky-blue-colored box) are carefully determined by a superimposed SP of three phases (Fig. 6). The important relationships among three phases (fcc matrix,  $\varepsilon_A$  and  $\varepsilon_{New}$ ) are  $[01\bar{1}0]_{\varepsilon_A} \parallel [11\bar{2}]_{fcc}$ ,  $[01\bar{1}1]_{\varepsilon_{New}} \parallel [112]_{fcc}$  and  $[0\bar{1}12]_{\varepsilon_A} \parallel [02\bar{2}3]_{\varepsilon_{New}}$ . Considering the slip systems of hcp and fcc structures, it is worthwhile to note that the directional trace of Shockley partial dislocation of fcc matrix ( $\langle 112 \rangle$ ) is parallel to those of partial  $\langle a \rangle$  dislocation of  $\varepsilon_A$  (blue-dotted horizontal line,  $\langle 01\bar{1}0 \rangle$ ) and to pyramidal I dislocation of  $\varepsilon_{New}$  (red-dotted diagonal line,  $\langle 01\bar{1}1 \rangle$ ), respectively. And, the directional parallelism between  $\varepsilon_A$  and  $\varepsilon_{New}$  is determined to be  $[0\bar{1}12]_{\varepsilon_A} \parallel [02\bar{2}3]_{\varepsilon_{New}}$  (green line), which implies that the direction of partial pyramidal I in  $\varepsilon_A$  is parallel to that of partial pyramidal II in  $\varepsilon_{New}$ . From the SP, we find that the parallelism between  $\varepsilon_A$  and fcc matrix corresponds to their Shoji-Nishiyama OR, and further the martensitic nucleation of  $\varepsilon_{New}$  from  $\varepsilon_A$  is strongly dependent on the pyramidal dislocation of both  $\varepsilon_A$  and  $\varepsilon_{New}$ . Therefore, the rotational relationship between  $\varepsilon_A$  and  $\varepsilon_{New}$  provides important experimental evidence in which the cross slip of two hcp martensites operates. Our ABF-STEM observation together with SP analyses on atomic configuration inducing formation of  $\varepsilon_{New}$  reveals that the directions of  $\langle c+a \rangle$  dislocations on  $\varepsilon_A$  and  $\varepsilon_{New}$  are mutually parallel to each other, namely the energy barrier against the formation of  $\varepsilon_{New}$  might be relatively smaller than those from pyramidal I plane into other slip systems within  $\varepsilon_A$ : (i) glissile-to-sessile transformation ( $\langle c+a \rangle \rightarrow \langle c \rangle + \langle a \rangle$ ) [3] or (ii) cross-slip from pyramidal I to pyramidal II plane inside  $\varepsilon_A$  [16].

### 3. 4 Dislocation model for $\epsilon_{\text{New}}$ nucleation based on two-beam analyses

To precisely determine the Burgers vectors of dislocations involved in the formation of  $\epsilon_{\text{New}}$  together with their slip systems, we performed  $\vec{g} \cdot \vec{b}$  analyses (where  $\vec{g}$  is the diffraction vector and  $\vec{b}$  is the Burgers vector,  $\vec{g} \cdot \vec{b}$  values for  $\langle a \rangle$  and  $\langle c+a \rangle$  dislocation are given in Table 1). The angles between important planes and directions related to pyramidal dislocation in two zone axes ( $z = [2\bar{1}\bar{1}0]$  and  $z = [0001]$ ) calculated from SP are given in Table 2. Figs. 7a and 7b show two-beam TEM bright-field (BF) images under two  $\vec{g}$  vectors in  $z = [2\bar{1}\bar{1}0]$ . Experimental evidence in which  $\epsilon_{\text{New}}$  nucleates directly from the  $\epsilon_A$  is highlighted by yellow dotted square in the upper-right side of figures. Under  $\vec{g} = 0002$  (Fig. 7a), both pyramidal  $\langle c+a \rangle$  dislocations and  $\langle c \rangle$  dislocation are visible, whereas basal  $\langle a \rangle$  dislocations are out of contrast. It is evidenced that most of dislocations involved in the formation of  $\epsilon_{\text{New}}$  are dislocations with  $\langle c \rangle$  component ( $\langle c+a \rangle$  or  $\langle c \rangle$  dislocation). On the other hand, some of basal  $\langle a \rangle$  dislocations are in contrast under  $\vec{g} = 0\bar{1}12$  (Fig. 7b). From geometrical and energetic points of view, they are  $\langle a \rangle$  partial dislocations having Burgers vector of  $\vec{b} = \frac{1}{3} \langle 01\bar{1}0 \rangle$  because the dissociation of perfect  $\langle a \rangle$  dislocation into partial dislocations ( $\frac{1}{3} \langle 11\bar{2}0 \rangle \rightarrow \frac{1}{3} \langle 01\bar{1}0 \rangle + \frac{1}{3} \langle 10\bar{1}0 \rangle$ ) is energetically more favorable following Frank rule [1]. On the bases of these observations, it is confirmed that essential dislocations contributing to nucleating a new hcp martensite ( $\epsilon_{\text{New}}$ ) are dislocations having  $\langle c \rangle$  component, namely either  $\langle c \rangle$  or  $\langle c+a \rangle$  dislocation.

However, two-beam analyses only under  $z = [2\bar{1}\bar{1}0]$  alone are not enough to clearly

define the Burgers vectors of perfect or partial  $\langle c+a \rangle$  dislocations because both exhibit the same contrast under  $\vec{g} = 0002$  and  $\vec{g} = 0\bar{1}12$  (all visible conditions, as shown in Table 1). It is known that the dislocation morphology is dramatically changed during tilting the specimen, which implies that the Burgers vector and gliding plane can be more precisely determined from complementary observations on the same area in different zone axis. To that end, we tilted our specimen using high-tilting holder, while maintaining the same observation area, into  $z = [0001]$ . Shown in Figs. 8a and 8b) are two-beam BF images under  $\vec{g} = \bar{2}110$  and  $\vec{g} = \bar{1}2\bar{1}0$ , respectively. Although the dislocation viewed along  $z = [2\bar{1}\bar{1}0]$  looks like a single straight line in Figs. 7a and 7b, it exhibits a curvilinear shape composed of two dislocation segments. Comparing with Fig. 7, complex configuration of dislocation are better resolved under the zone axis of  $z = [0001]$  wherein three important regions requiring further attention to visualize dislocation model for nucleation of  $\varepsilon_{\text{New}}$  are highlighted. To determine the Burgers vectors and dislocation character of pyramidal dislocation appearing in Fig. 8, the analyses of SP under  $z = [0001]$  were carried out and is depicted in Fig. 9. Based on two-beam analyses and corresponding SP, the dislocation model to elucidate the formation of  $\varepsilon_{\text{New}}$  (Fig. 10) is summarized as follows.

**(Region I)** The edge-type pyramidal dislocation having Burgers vector of  $\vec{b} = \frac{1}{3}[11\bar{2}3]$  (determined by SP in Fig. 9a) is activated and subsequently dissociated into two partial dislocations on pyramidal I plane  $((0\bar{1}11))$  of  $\varepsilon_A$ :  $\frac{1}{3}[11\bar{2}3] \rightarrow \frac{1}{3}[10\bar{1}1] + \frac{1}{3}[0\bar{1}12]$ . The reason why the dissociation of pyramidal dislocation occurs primarily on pyramidal I over pyramidal II is due to the lower  $c/a$  value of our hcp martensite than ideal  $c/a$  ratio, as will be discussed later [3, 15-17, 23].



**(Region II)** The dissociated pyramidal partials, continuously glided on pyramidal I plane, start to pile up at the junction of pyramidal/basal planes of  $\varepsilon_A$  ( $\langle 2\bar{1}\bar{1}0 \rangle$  indicated by pink-dotted arrow along the line) whose contrast is distinguished as fragmented contrast (blue arrows). After close interaction of pyramidal-basal dislocations, the pile-up dislocations start to change their glide plane, namely the cross slip comes into picture, which is evidenced by V-shaped dense contrast having Burgers vectors of  $\frac{1}{3}[10\bar{1}1]$  (orange arrowheads in Fig. 8a) and  $\frac{1}{3}[0\bar{1}12]$  (yellow arrowheads in Fig. 8b) similar to the stair-rod dislocation connecting two close-packed  $\{111\}$  planes of fcc materials. The cross-slipped dislocations arrange themselves into a direction parallel to  $[01\bar{1}0]$ . The direction determined from SP in Fig. 9b corresponds to the intersection line of basal-pyramidal II plane of  $\varepsilon_{New}$  (red-dotted line). From the intersection line, the perfect pyramidal dislocation having a Burgers vector of  $\frac{1}{3}[11\bar{2}\bar{3}]$  starts to glide onto pyramidal II plane of  $\varepsilon_{New}$ .

**(Region III)** After cross-slip completed, newly formed pyramidal dislocation on pyramidal II plane ( $(2\bar{1}\bar{1}2)$ ) of  $\varepsilon_{New}$  also dissociate into two partials ( $\frac{1}{3}[11\bar{2}\bar{3}] \rightarrow \frac{1}{6}[02\bar{2}\bar{3}] + \frac{1}{6}[20\bar{2}\bar{3}]$ ) and further glides along the plane, which brings forth the embryo of  $\varepsilon_{New}$ . When side-on viewed along  $z = [2\bar{1}\bar{1}0]$ , the two hexagons corresponding to  $\varepsilon_A$  and  $\varepsilon_{New}$  martensites in Fig. 10 have the same atomic configuration as that observed using ABF-STEM as shown in Fig. 5a.

## 4. Discussion

### 4. 1 Slip pathway and cross slip of hcp martensite

The plasticity of hcp-based materials is intimately related to the fundamental behaviors of pyramidal  $\langle c+a \rangle$  dislocations, which are the major contributor to c-axis strain, and thus, the high ductility in hcp structure is achievable by generating more  $\langle c+a \rangle$  dislocations [3, 15-17, 23]. Among various material parameters, the  $c/a$  ratio plays an important role in determining the slip pathway of hcp structure: non-basal pyramidal  $\langle c+a \rangle$  slip and deformation twinning modes, which are crucial for accommodating higher strain along c-axis and associated work hardening behavior [17]. Although  $c/a$  ratio as an intrinsic material parameter remains constant when alloy composition is fixed, Sinha *et al.* [23] tried to change the  $c/a$  ratio of hcp martensite in high entropy alloy (HEA) by tuning the transformation volume and showed that lower than ideal  $c/a$  ratio promotes non-basal pyramidal  $\langle c+a \rangle$  slip and deformation twinning. Furthermore, Wu and Curtin [17] using MD simulations showed that the primary slip plane of hcp metals also show strong dependency on  $c/a$  ratio: the  $\langle c+a \rangle$  dislocation is energetically preferable on pyramidal I for Ti, Zr, and Re ( $c/a < 1.633$ ), and on pyramidal II for Zn and Cd ( $c/a > 1.633$ ). In Mg whose  $c/a$  is close to ideal value, the energy difference between pyramidal I and II is small and thus cross slip is easily activated. Based on neutron diffraction experiments coupled with Rietveld refinement [20], the lattice parameter of our hcp martensite was measured to be  $a = 2.5484$  and  $c = 4.1081$  Å and corresponding  $c/a$  ratio was 1.612 (below ideal  $c/a=1.633$ ). Therefore, it is conceivable that the activation of  $\langle c+a \rangle$  slip can be favorable in our hcp martensite, and the  $\langle c+a \rangle$  dislocation can dissociate into partials preferentially on

pyramidal I over pyramidal II.

Cross-slip is a crucial process in plasticity, acting to spread slip spatially on multiple non-parallel planes and to enable dislocation multiplication and annihilation processes; all of these processes affect ductility and strength of the material. Whereas the atomistic mechanisms, energy barriers, and rates of cross-slip are well established in cubic metals, the mechanisms in materials with hcp structure are still under controversy [3, 15-17, 23]. Liu *et al.* [16] using 3D TEM tomography showed that cross slip of perfect  $\langle c+a \rangle$  dislocation, instead of partial  $\langle c+a \rangle$  dislocations, took place between pyramidal I and II planes. The cross slip of perfect  $\langle c+a \rangle$  dislocation in hcp martensite was also confirmed in HEA [23]. On the other hand, recent atomistic simulations showed that cross slip proceeded by the individual dissociated partials rather than perfect-type  $\langle c+a \rangle$  dislocation [3]. In our investigation, the close interaction of the pyramidal dislocation with gliding  $\langle a \rangle$  dislocation makes cross-slip possible whose dislocation reaction can be expressed:  $\frac{1}{3} \langle 0\bar{1}\bar{1}\bar{2} \rangle + \frac{1}{3} \langle 1\bar{1}0\bar{1} \rangle + \frac{1}{3} \langle 1100 \rangle = \frac{1}{3} \langle 2\bar{1}\bar{1}\bar{3} \rangle$ . Once the cross slip took place, another component of pyramidal dislocation was also activated by changing gliding direction and started to dissociate into easy-gliding partials having Burgers vectors of  $\frac{1}{6} [02\bar{2}\bar{3}]$  and  $\frac{1}{6} [20\bar{2}\bar{3}]$  along pyramidal II plane ( $(2\bar{1}\bar{1}2)$ ) of  $\varepsilon_{\text{New}}$ . Therefore, our TEM examination confirmed that cross slip is realized by dissociated partial dislocations rather than perfect dislocation. We consider that the dissociation and concurrent cross slip is energetically more favorable because the  $b^2$  value of  $\langle c+a \rangle$  perfect dislocation is quite larger compared with those of partials. As already addressed, the two perfect  $\langle c+a \rangle$  dislocations that glide on pyramidal I plane of  $\varepsilon_A$  and on pyramidal II of  $\varepsilon_{\text{New}}$  are almost parallel to each other, implying the cross-slip of this route is energetically more favorable than switching into

other slip systems: either (i) glissile-to-sessile transformation ( $\frac{1}{3} \langle 1\bar{2}13 \rangle \rightarrow \langle 0001 \rangle + \frac{1}{3} \langle 1\bar{2}10 \rangle \rightarrow \langle 0001 \rangle + \frac{1}{3} \langle 1\bar{1}00 \rangle + \frac{1}{3} \langle 0\bar{1}10 \rangle$ ) [3] or (ii) cross-slip from pyramidal I to pyramidal II plane of  $\varepsilon_A$  itself ( $\frac{1}{3} \langle 1\bar{2}13 \rangle_{0\bar{1}11} \cdot \frac{1}{3} \langle 1\bar{2}12 \rangle \rightarrow \frac{1}{3} \langle 1\bar{1}01 \rangle_{(0\bar{1}11)} + \frac{1}{3} \langle 0\bar{1}12 \rangle_{(0\bar{1}11)} \rightarrow \frac{1}{6} \langle 0\bar{2}23 \rangle_{(1\bar{2}12)} + \frac{1}{6} \langle 2\bar{2}03 \rangle_{(1\bar{2}12)}$ ) [16].

## 4. 2 For the consilience of deformation scenario

The SFE landscape has been regarded as a governing factor to determine the entire plasticity of fcc-based materials [18-20]. The SFE of the investigated material was measured by two-step approach of line profile analyses (Rietveld whole-profile fitting followed by double-Voigt size-strain analyses) on neutron diffraction profiles in our previous investigation and the measured SFE was 10.4 mJ/m<sup>2</sup> [20]. Although it provides a practical guideline in search of favored deformation structure (MT, twinning and slip), the disagreements regarding the criterion to distinguish each deformation mode and the large scatters of measured SFE certainly point to the need for further research revealing additional factor [9, 21]. In addition to SFE concept, here, we go one step further to turn our attention into other important factors underlying deformation mechanism by categorizing the stage of deformation into first- and second-order hierarchy.

### 4. 2. 1 First-order hierarchy

The governing factor in this stage is ***the dissociation routes of perfect dislocation and resulting predominant types of partial dislocations in fcc matrix***. The possible routes for dissociation of perfect dislocation and corresponding dislocation reactions are summarized in

Fig. 11. When a perfect dislocation will not dissociate into partial dislocations, conventional slip by glide of undissociated perfect dislocation governs the plasticity of fcc materials (**Route 0**: the SFE is highest). When a perfect dislocation with  $\vec{b} = \frac{1}{2}[\bar{1}01]$  dissociates into Frank and Shockley partials, the fcc-to-hcp ( $\epsilon_A$ ) MT indeed operates (**Route I**: the SFE is lowest below 20 mJ/m<sup>2</sup>). In this event, screw-type perfect dislocation induced the torsional flow of {111} planes of fcc matrix (Eshelby twist [25]) and its dissociation provides a self-perpetuating step to bring forth Frank partial acting as a critical component to accomplish every other periodicity required for fcc-to-hcp MT [21]. When the perfect dislocation dissociates into two Shockley partials only (**Route II**: the SFE is medium), the deformation twinning is predominant, known as three-layer twin model [26, 27]. It is worthwhile to note that, although MT and twinning have different character in nature, the previous models [26-36] to elucidate their formation mechanisms have tied with the partial-dislocation types induced by dissimilar dissociation routes, apart from SFE concept. By incorporating these models whose discussions are concentrated on the operation of specific types of partial dislocation into SFE concept, we demonstrate how dissociation routes of perfect dislocation can be exploited to determine deformation mechanism (MT, twinning, slip), which can provide more practical guideline of first-order hierarchy in deformation scenario of fcc materials (Fig. 12a).

#### 4. 2. 2 Second-order hierarchy

After fcc-to-hcp MT governs the first-order hierarchy of deformation mechanism, the governing factor for subsequent second-order hierarchy is ***the dislocation plasticity of hcp martensite per se*** (Fig. 12b). (**Stage I: formation of  $\epsilon_{New}$** ) Our current investigation showed that the formation of  $\epsilon_{New}$  can be understood by dislocation reaction inside  $\epsilon_A$ , i.e., (i) the

activation of pyramidal dislocation and its dissociation on pyramidal I plane of  $\varepsilon_A$ , (ii) their interaction with gliding basal  $\langle a \rangle$  dislocations and pile-up at the pyramidal/basal junction, and (iii) cross slip of pile-up dislocations into pyramidal II plane of  $\varepsilon_{\text{New}}$ . (**Stage II: hcp-to-bcc MT**)

The occurrence of stage I or II depends on whether the intersection of independently-operated hcp martensites occurs or not. Two different hcp martensites ( $\varepsilon_A$  and  $\varepsilon_B$ ) have separately nucleated on different close-packed planes of fcc matrix (e.g., (111) and  $(1\bar{1}1)$ ) via fcc-to-hcp MT model [21], and (ii) their subsequent intersection (collision) leads to the formation of bcc martensite. During the intersection (collision) of two hcp martensites ( $\varepsilon_A$  and  $\varepsilon_B$ ), the lattice distortion responsible for the hcp-to-bcc MT was observed. That is, the partial dislocation parallel to  $[0\bar{1}10]$  in moving  $\varepsilon_B$  approaches partial dislocation having  $[10\bar{1}0]$  direction in stationary  $\varepsilon_A$ , resulting in the formation of a stair-rod dislocation with  $[2\bar{1}\bar{1}0]$  direction which connects two hcp variants ( $\frac{1}{3}[1\bar{1}00]_{(0001)\varepsilon_B} + \frac{1}{3}[10\bar{1}0]_{(0001)\varepsilon_A} \rightarrow \frac{1}{3}[2\bar{1}\bar{1}0]_{\varepsilon_B \rightarrow \varepsilon_A}$ ) [22]. This is similar to the Route III in which stair-rod dislocation plays an important role in plasticity of fcc materials. Since the hcp-to-bcc MT takes place at the intersection area of two hcp martensites, the the area that has not experienced intersection remains hcp crystals, as indicated Stage II in Fig. 12.

## 5. Conclusions

In summary, the pyramidal dislocation played a key role in plasticity of Fe-based hcp martensite. The formation of new hcp martensite ( $\varepsilon_{\text{New}}$ ) can be explained by dislocation reaction inside primary hcp martensite ( $\varepsilon_A$ ) formed via fcc-to-hcp MT, i.e., (i) the activation of

pyramidal dislocation and its dissociation on pyramidal I plane of  $\varepsilon_A$ , (ii) their interaction with gliding basal  $\langle a \rangle$  dislocations and pile-up at the pyramidal/basal junction, and (iii) cross slip of pile-up dislocations into pyramidal II plane of  $\varepsilon_{New}$ . By incorporating our current model into previous models and SFE concept, we suggested a consilience of deformation scenario of fcc-based materials by categorizing the stage of deformation into first- and second-order hierarchy. The governing factors to categorize the first-order and second-order hierarchy of deformation mechanism are (1) the dissociation route of perfect dislocation and resulting partial dislocation component and (2) the dislocation plasticity of hcp martensite itself. Our experimental and theoretical approaches can provide not only in-depth understanding on the nature of plasticity and transformability in crystals with close-packed structure but also a powerful platform for designing high-performance materials with enhanced damage tolerance and shape recoverability.

## References

1. D. Hull, D. J. Bacon, Introduction to Dislocations 5th edn (Butterworth-Heinemann, 2011).
2. D. Raabe, C. C. Tasan, E. A. Olivetti, Strategies for improving the sustainability of structural metals, *Nature* 575 (2019) 64–74.
3. Z. Wu, W. A. Curtin, The origins of high hardening and low ductility in magnesium, *Nature* 526 (2015) 62-67.
4. R. O. Ritchie, The conflicts between strength and toughness, *Nature Mater.* 10 (2011) 817-822.
5. Y. M. Wang, T. Voisin, J. T. McKeown, J. Ye, N. P. Calta, Z. Li, Z. Zeng, W. Zhang, T. T. Roehling, R. T. Ott, M. K. Santala, P. J. Depond, J. Matthews, A. V. Hamza, T. Zhu, additively manufactured hierarchical stainless steels with high strength and ductility, *Nature Mater.* 17 (2017) 63-73.
6. Z. Nishiyama, Martensitic transformation (Academic Press Inc., 1971).
7. G. B. Olson, M. Cohen, A perspective on martensitic nucleation, *Ann. Rev. Mater. Sci.* 11 (1981) 1-30.
8. E. Pereloma, D. V. Edmonds, Phase transformation in steels (Woodhead Publishing Series in Metals and Surface Engineering, 2012).
9. G. M. Bellefon, J. C. Duysen, Tailoring plasticity of austenitic stainless steels for nuclear applications: Review of mechanisms controlling plasticity of austenitic steels below 400 °C, *J. Nuclear Mater.* 475 (2016) 168-191.



10. M. Soleimani, A. Kalhor, H. Mirzadeh, Transformation-induced plasticity (TRIP) in advanced steels: a review, *Mater. Sci. Eng. A* 795 (2020) 140023.
11. Y. Tanaka, Y. Himuro, R. Kainuma, Y. Sutou, T. Omori, K. Ishida, Ferrous polycrystalline shape-memory alloy showing huge superelasticity, *Science* 327 (2010) 1488-1490.
12. P. Chowdhury, H. Sehitoglu, Deformation physics of shape memory alloys - Fundamentals at atomistic frontier, *Prog. Mater. Sci.* 88 (2017) 49-88.
13. A. J. Bogers, W. G. Burgers, Partial dislocations on the {110} planes in the bcc lattice and the transition of the fcc into the bcc lattice, *Acta Metall.* 12 (1964) 255-261.
14. M. H. Yoo, Slip, Twinning and Fracture in hexagonal close-packed metals, *Metall. Trans.* 12A (1981) 409-418.
15. Z. Wu, R. Ahmad, B. Yin, S. Sandlöbes, W. A. Curtin, Mechanistic origin and prediction of enhanced ductility in magnesium alloys, *Science* 359 (2018) 447-452.
16. B.-O. Liu, F. Liu, N. Yang, X.-B. Zhai, L. Zhang, Y. Li, B. Yang, J. Li, E. Ma, J.-F. Nie, Z.-W. Shan, Large plasticity in magnesium mediated by pyramidal dislocations, *Science* 365 (2019) 73-75.
17. Z. Wu, B. Yin, W. A. Curtin, Energetics of dislocation transformations in hcp metals, *Acta Mater.* 119 (2016) 203-217.
18. H. V. Swygenhoven, P. M. Derlet, A. G. Frøseth, Stacking fault energies and slip in nanocrystalline metals, *Nature Mater.* 3 (2004) 399-403.
19. L. Remy, A. Pineau, Twinning and strain-induced FCC→HCP transformation on the mechanical properties of Co-Ni-Cr-Mo alloys, *Mater. Sci. Eng.* 26 (1976) 123-132.
20. T.-H. Lee, E. Shin, C.-S. Oh, H.-Y. Ha, S.-J. Kim, Correlation between stacking fault energy

- and deformation microstructure in high-interstitial-alloyed austenitic steels, *Acta Mater.* 58 (2010) 3173-3186.
21. T.-H. Lee, S.-D. Kim, H.-Y. Ha, J. H. Jang, J. Moon, J.-Y. Kang, C.-H. Lee, S.-J. Park, W. Woo, J.-H. Shin, J.-W. Lee, D. W. Suh, H.-U. Hong, Screw dislocation driven martensitic nucleation: A step toward consilience of deformation scenario in fcc materials, *Acta Mater.* 174 (2019) 342-350.
22. T.-H. Lee, H.-Y. Ha, J.-Y. Kang, J. Moon, C.-H. Lee, S.-J. Park, An intersecting-shear model for strain-induced martensitic transformation, *Acta Mater.* 61 (2013) 7399-7410.
23. S. Sinha, S. S. Nene, M. Frank, K. Liu, P. Agrawal, R. S. Mishra, On the evolving nature of c/a ration in a hexagonal close-packed epsilon martensite phase in transformative high entropy alloys, *Sci. Reports.* 9 (2019) 13185.
24. P. Hirsch, D. Cockayne, J. Spence, M. Whelan, 50 years of TEM of dislocations: past, present and future, *Philos. Mag.* 86 (2006) 4519–4528.
25. M. J. Bierman, Y. K. A. Lau, A. V. Kvit, A. L. Schmitt, Jin Song, Dislocation-Driven Nanowire Growth and Eshelby Twist, *Science*, 320, 1060-1063 (2008).
26. J. W. Christian, S. Mahajan, Deformation Twinning. *Prog. Mater. Sci.* 39, 1-157 (1995).
27. T.-H. Lee, C.-S. Oh, S.-J. Kim, S. Takaki, Deformation twinning in high-nitrogen austenitic stainless steel, *Acta Mater.* 55 (2007) 3649-3662.
28. W. Bollmann, On the phase transformation of cobalt, *Acta Metall.* 9 (1961) 972-975.
29. A. Seeger, Versetzungen und allotrope Umwandlungen, *Z. Metallk.* 44 (1953) 247-253.
30. J. A. Venable, The martensite transformation in stainless steel, *Philos. Mag.* 7 (1962) 35-44.

31. S. Mahajan, M. L. Green, D. Brasen, A model for the fcc→hcp transformation, its applications, and experimental evidence, *Metall. Trans.* 8A (1977) 283-293.
32. H. Fujita, S. Ueda, Stacking faults and fcc→hcp transformation in 18/8 type stainless steel, *Acta Metall.* 20 (1972) 759-767.
33. J. Venables, Deformation Twinning in Face-Centred Cubic Metals, *Phil. Mag.* 6 (1961) 379-396.
34. J. Venables, On Dislocation Pole Models for Twinning, *Phil. Mag.* 30 (1974) 1165-1169.
35. S. Mahajan, G. Chin, Formation of Deformation Twins in Fcc Crystals, *Acta Metall.* 21 (1973) 1353-1363.
36. T. Mori, H. Fujita, Dislocation reactions during deformation twinning in Cu-11at.% Al single crystals, *Acta Metall.* 28 (1980) 771-776.

## **Acknowledgements**

This work was supported financially by the Fundamental Research Program of Korean Institute of Materials Science (PNK9820 and PKC2130). One of the authors (THL) also would like to thank Late Y.O. Kim at Han-Yang University, Prof. S.D. Kim at Pukyong National University and Mr. S.H. Han at KIMS for their help with the TEM characterization.

## **Author contributions**

**Tae-Ho LEE:** Conceptualization, Writing – Review & Editing, Writing – Original Draft and Investigation.

**Heon-Young HA:** Conceptualization, Data Curation, Validation and Resources.

**Seong-Hoon KIM:** Formal analysis and Resources.

**Hyung-Kwon PARK:** Validation and Investigation.

**Seong-Jun PARK:** Validation and Investigation.

**Chang-Hoon LEE:** Investigation and Project administration.

**Subin LEE:** Visualization and Investigation.

**Christoph Kirchlechner:** Supervision and Writing – Review & Editing.

< Figure caption >


**Fig. 1** Conventional and high-resolution (HR) TEM images of (a) the first-order (fcc-to-hcp) and (b)-(c) the second-order hierarchy of martensitic transformation (MT). The true stress ( $\sigma_t$ ) versus true strain ( $\epsilon_t$ ) curve and the change in volume fraction of constituting phases (fcc austenite matrix, hcp martensite and bcc martensite) are shown together.

**Fig. 2** Schematic illustration to visualize three different types of hcp martensite formed during tensile deformation: (a) the fcc-to-hcp ( $\epsilon_A$ ) MT [21]. (b) activation of conjugate variant of hcp martensite ( $\epsilon_B$ ), (c) hcp-to-bcc MT via intersection of two hcp martensites ( $\epsilon_A$  and  $\epsilon_B$ ) [22]., and (d) autocatalytic formation of  $\epsilon_{New}$  **without** intersection of two hcp martensites.

**Fig. 3** Dislocation motion inside  $\epsilon_A$  revealed by in-situ TEM: (a) to (c) snapshots obtained from in-situ TEM straining showing nucleation of  $\epsilon_{New}$  out of initially formed  $\epsilon_A$ . (a) 45s, (b) 69s and (c) 70s.

**Fig. 4** (a) The important pyramidal slip systems of hcp martensite showing pyramidal I (blue) and pyramidal II slip (red). (b) Crystallographic information of hcp martensite evaluated from Rietveld refinement on neutron diffraction profile [22].

**Fig. 5** Annular bright field (ABF) STEM and geometric phase analysis (GPA) for elucidating the

nucleation of  $\varepsilon_{\text{New}}$ . (a) ABF-STEM image showing nucleation of  $\varepsilon_{\text{New}}$ . The change in stacking sequence (ABAB  CBCB) by introduction of stacking fault (SF) and the rotational relationship between  $\varepsilon_A$  and  $\varepsilon_{\text{New}}$  are highlighted in the bottom of (a). (b) The  $\varepsilon_{xy}$  strain map obtained from GPA analysis. (c) Burgers circuit (orange arrow) for determination of edge dislocation (blue arrow) in comparison with regular hcp lattice (white arrow) in overlaid image of ABF and GPA.

**Fig. 6** The superimposed stereographic projection of three phases,  $\varepsilon_A$  whose important slip systems are indicated in the below of SP,  $\varepsilon_{\text{New}}$  (yellow-colored box) and fcc matrix (sky-blue-colored box) ( $z = [1\bar{1}0]_Y \parallel [2\bar{1}\bar{1}0]_{\varepsilon_A}$ ). The Burgers vector ( $\frac{1}{3}[0\bar{1}11]$  of  $\varepsilon_A$ ) and dislocation line of pyramidal dislocation responsible for the formation of  $\varepsilon_{\text{New}}$  (orange-dotted arrow).

**Fig. 7** Two-beam analyses to determine the dislocation configuration involved in the formation of  $\varepsilon_{\text{New}}$ , (a)  $\vec{g} = 0002$  and (b)  $\vec{g} = 0\bar{1}12$  under  $z = [2\bar{1}\bar{1}0]$ .

**Fig. 8** Two-beam analyses to determine the dislocation configuration involved in the formation of  $\varepsilon_{\text{New}}$ , (a)  $\vec{g} = \bar{2}110$  and (b)  $\vec{g} = \bar{1}2\bar{1}0$  under  $z = [0001]$ . The important region to visualize the dislocation model for nucleation of  $\varepsilon_{\text{New}}$  are highlighted in green circle (**Region I**), orange-dotted box (**Region II**) and yellow-dotted box (**Region III**) in Figs. 7 and 8.

**Fig. 9** (a) Stereographic projection to determine the Burgers vector and dislocation character of pyramidal dislocation appearing in Fig. 8(a) (green-dotted arrow). (b) Stereographic

projection to trace the basal-pyramidal intersection line (red-dotted line) ( $z = [0001]$  of  $\varepsilon_{\text{New}}$ ).

**Fig. 10** Dislocation model for nucleation of new hcp martensite: (Left) the initial dissociation of pyramidal  $\langle c+a \rangle$  in pyramidal I plane and pile-up at the interface of pyramidal / basal junction within  $\varepsilon_A$ ; (Right) cross slip of dissociated  $\langle c+a \rangle$  from pyramidal I of  $\varepsilon_A$  onto pyramidal II of  $\varepsilon_{\text{New}}$ , resulting in the formation of  $\varepsilon_{\text{New}}$ .

**Fig. 11** Dissociation routes of perfect dislocation and corresponding dislocation reactions in fcc materials.

**Fig. 12** Deformation scenario for first- and second-order of MT. (a) The first-order hierarchy (The increasing trend of SFE value (from top to bottom) is indicated by green arrow). The governing factor is the dissociation route of perfect dislocation and resulting partial dislocation components (Fig. 11). (b) The second-order hierarchy of MT. The governing factor is the dislocation plasticity of hcp martensite itself. (Stage I) formation of  $\varepsilon_{\text{New}}$ , and (Stage II) hcp-to-bcc MT via the intersection of two hcp martensites ( $\varepsilon_A$  and  $\varepsilon_B$ ).

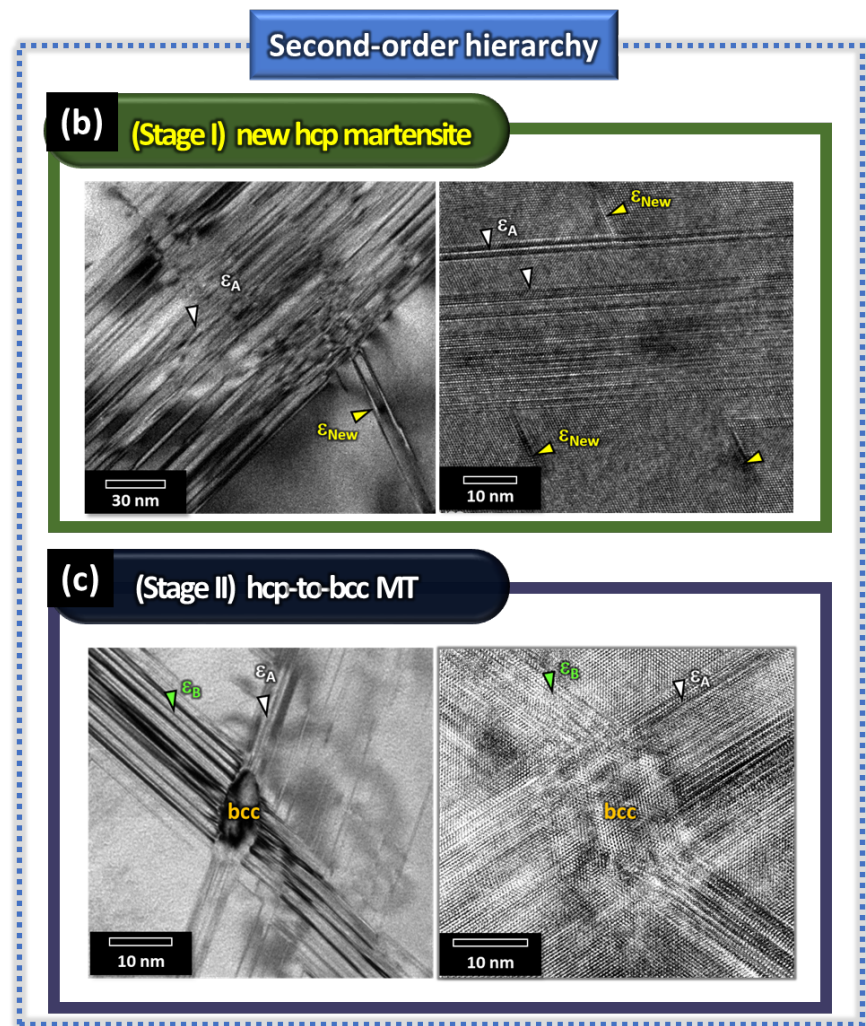
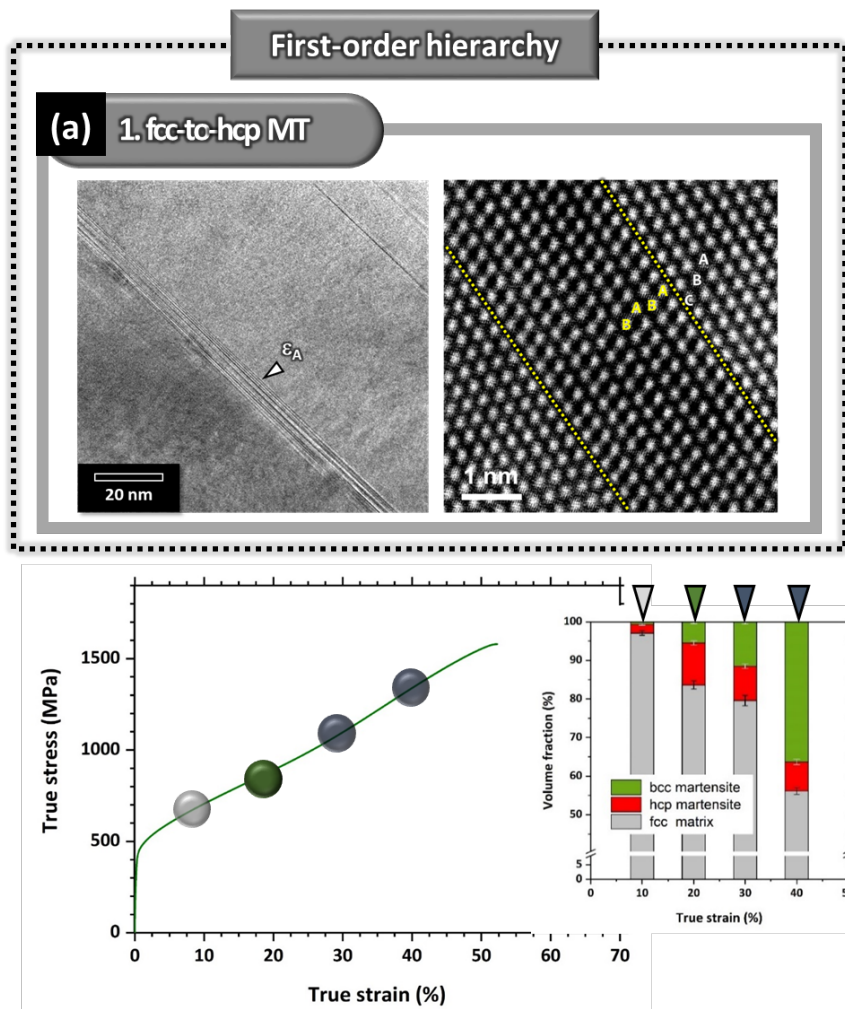


Fig. 1



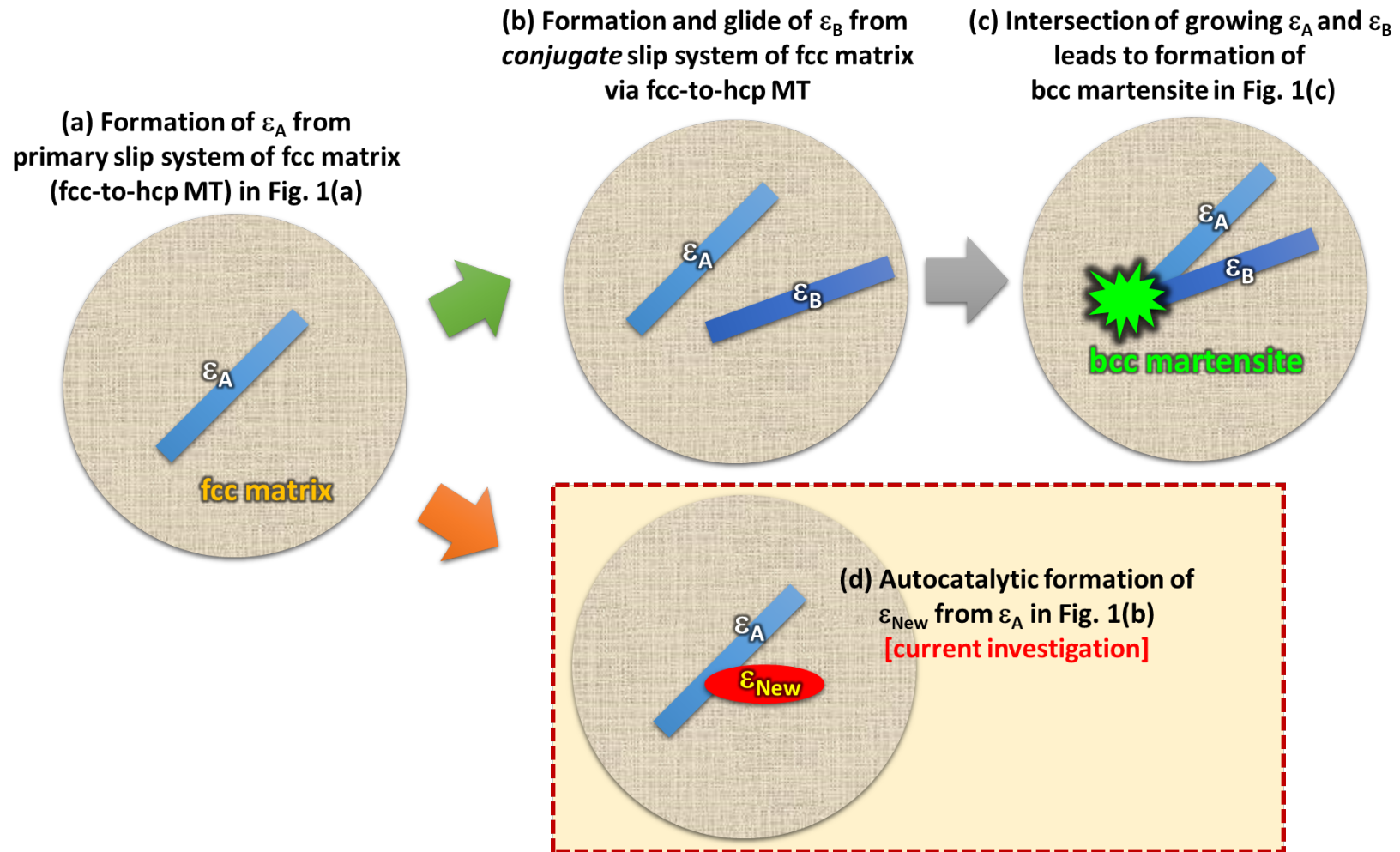


Fig. 2

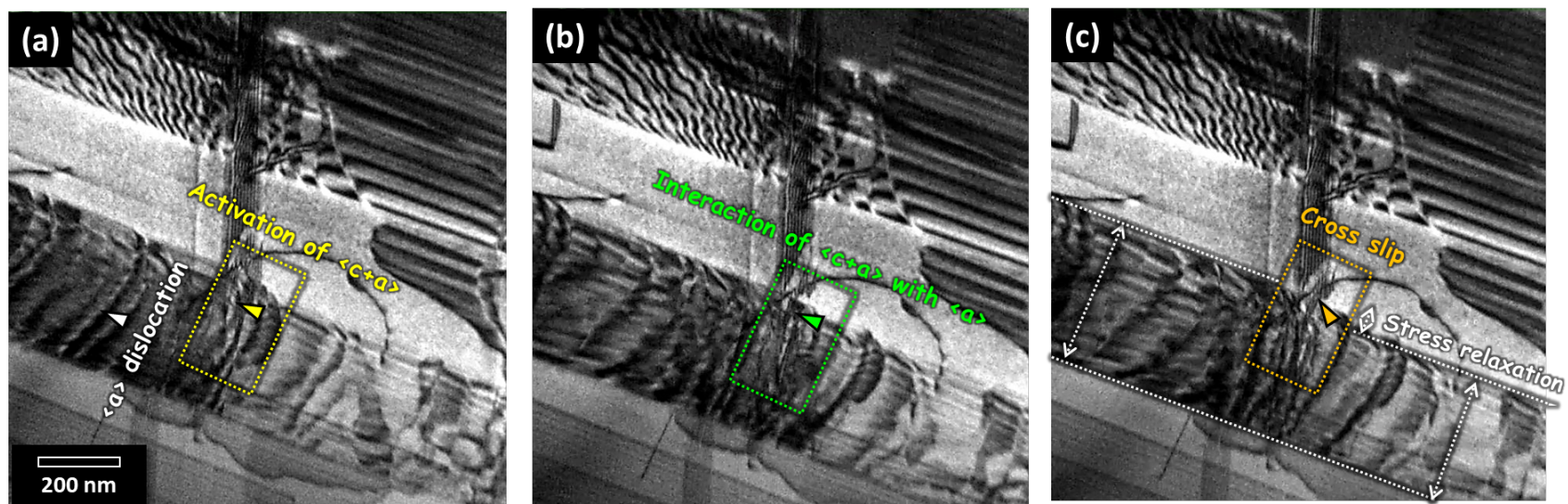
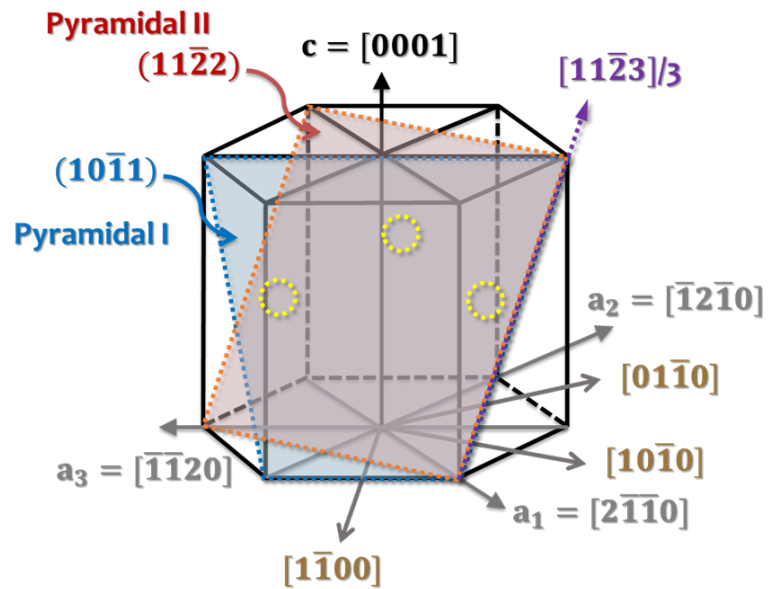


Fig. 3



(a)

Crystal structure: hcp (Space group: P63/mmc)

Lattice parameter:  $a=2.5484$  (Å),  $c=4.1217$  (Å);  $c/a=1.6174$

h	k	i	l	Mult	D spacing (Å)	2θ (degree)	Note
1	0	-1	0	6	2.206962	49.137	1 <sup>st</sup> order Prismatic plane
0	0	0	2	2	2.060835	52.88	Basal plane
1	0	-1	1	12	1.945604	56.281	1 <sup>st</sup> order Pyramidal plane
1	0	-1	2	12	1.506242	75.065	
1	1	-2	0	6	1.27419	92.135	2 <sup>nd</sup> order Prismatic plane
1	0	-1	3	12	1.166352	103.764	
2	0	-2	0	6	1.103481	112.519	
1	1	-2	2	12	1.083767	115.707	2 <sup>nd</sup> order Pyramidal plane
2	0	-2	1	12	1.06594	118.824	
0	0	0	4	2	1.030417	125.879	

(b)

Fig. 4

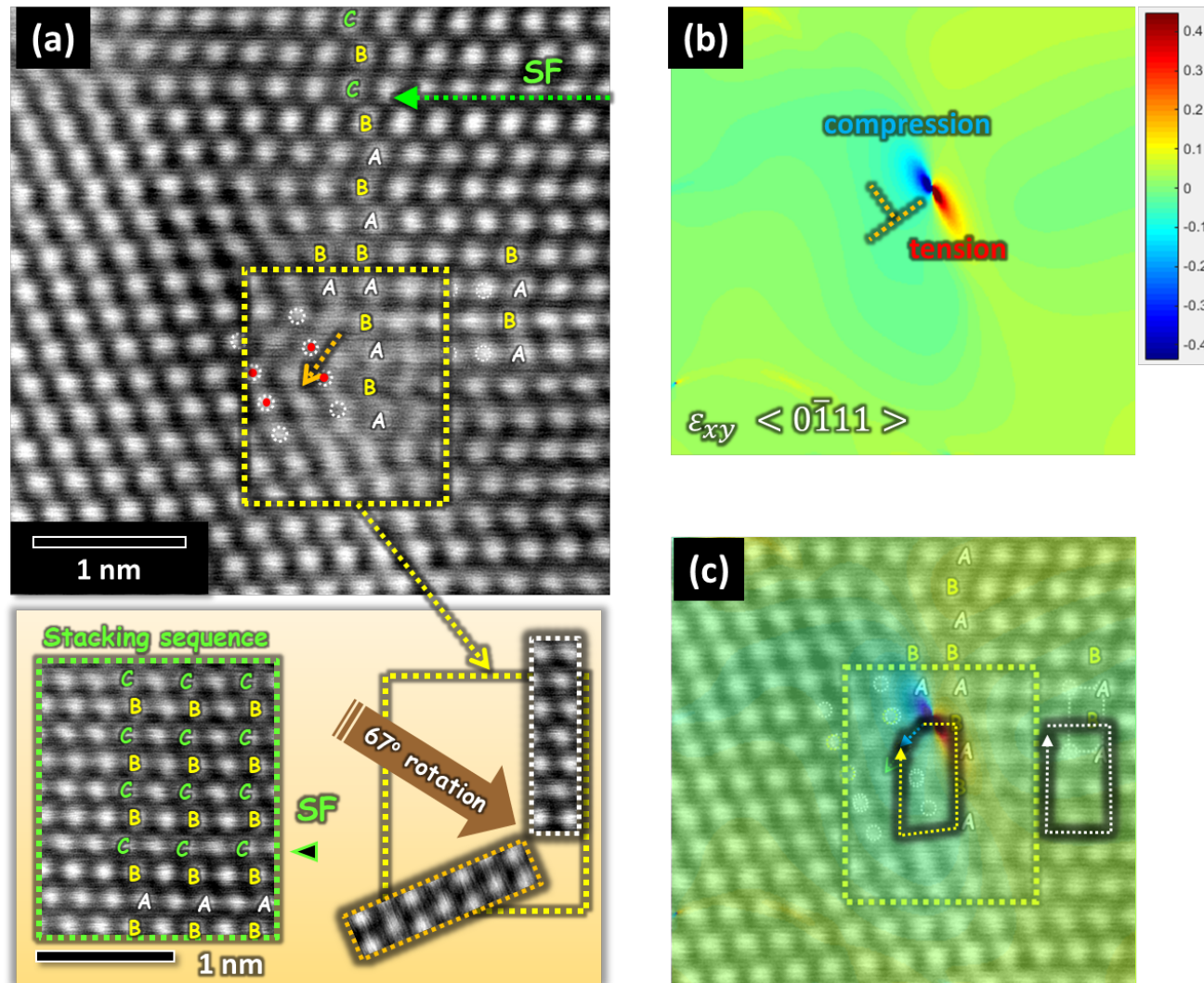


Fig. 5

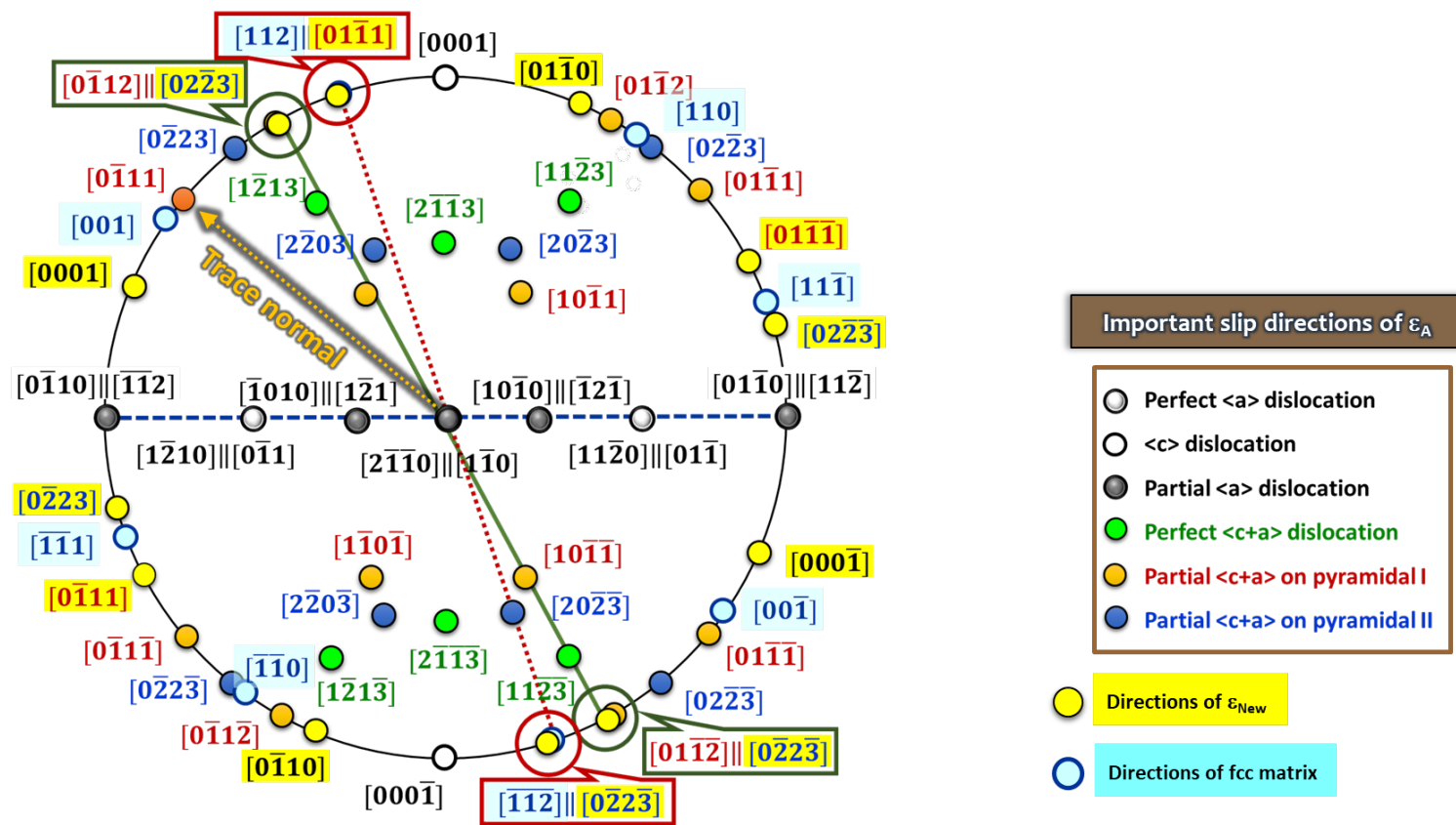


Fig. 6



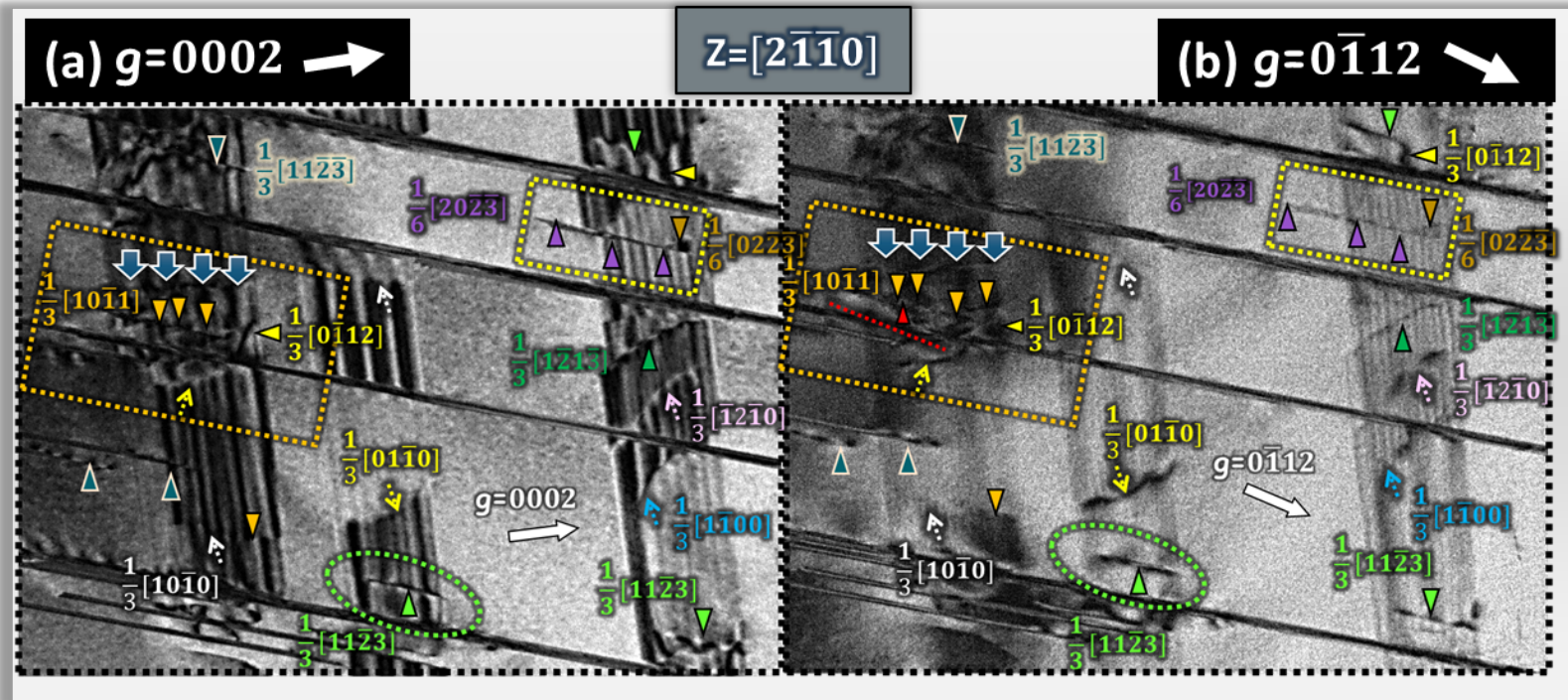


Fig. 7

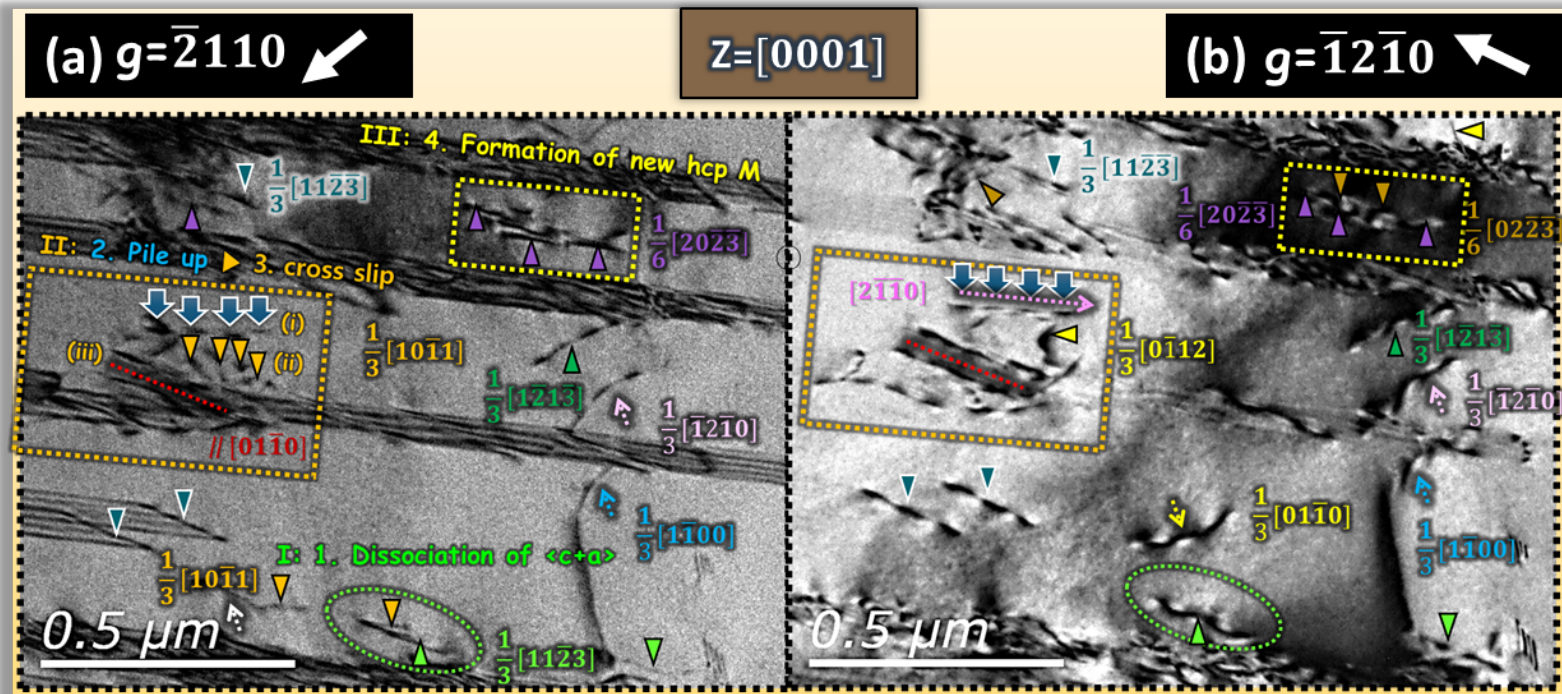
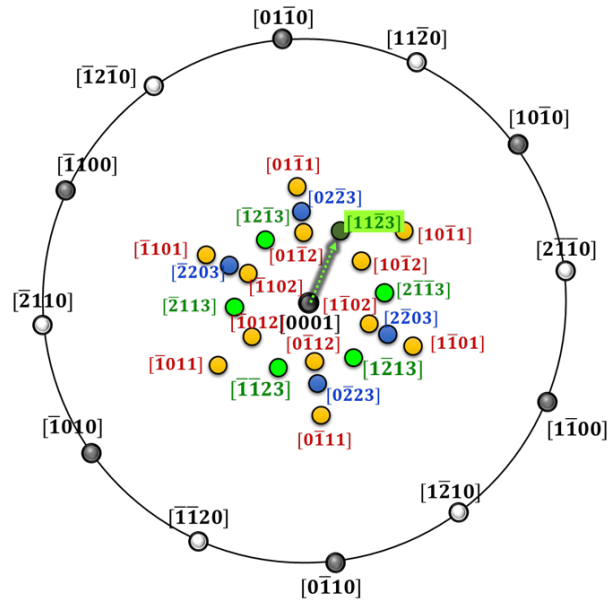


Fig. 8

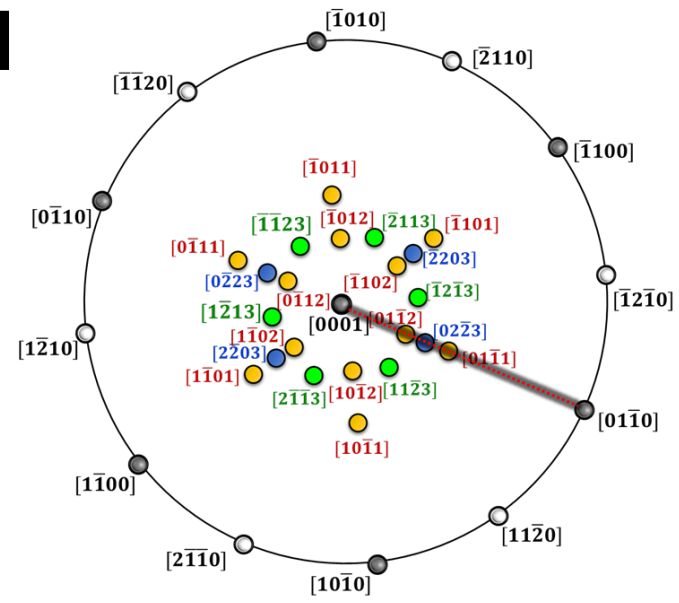
(a)



Important directions of  $\varepsilon_A$

- Perfect <a> dislocation
- <c> dislocation
- Partial <a> dislocation
- Perfect <c+a> dislocation
- Partial <c+a> on pyramidal I
- Partial <c+a> on pyramidal II

(b)



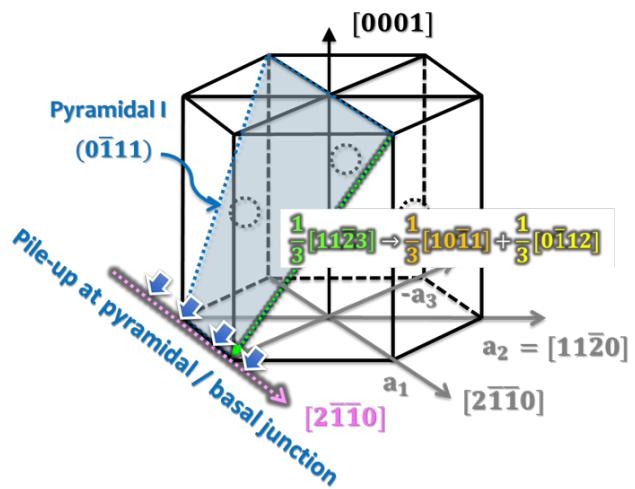
Important directions of  $\varepsilon_{New}$

- Perfect <a> dislocation
- <c> dislocation
- Partial <a> dislocation
- Perfect <c+a> dislocation
- Partial <c+a> on pyramidal I
- Partial <c+a> on pyramidal II

Fig. 9



### 1. Dissociation on pyramidal I of $\varepsilon_A$ and pile-up along $[2\bar{1}\bar{1}0]$



### 2. Cross-slip and formation of $\varepsilon_{New}$

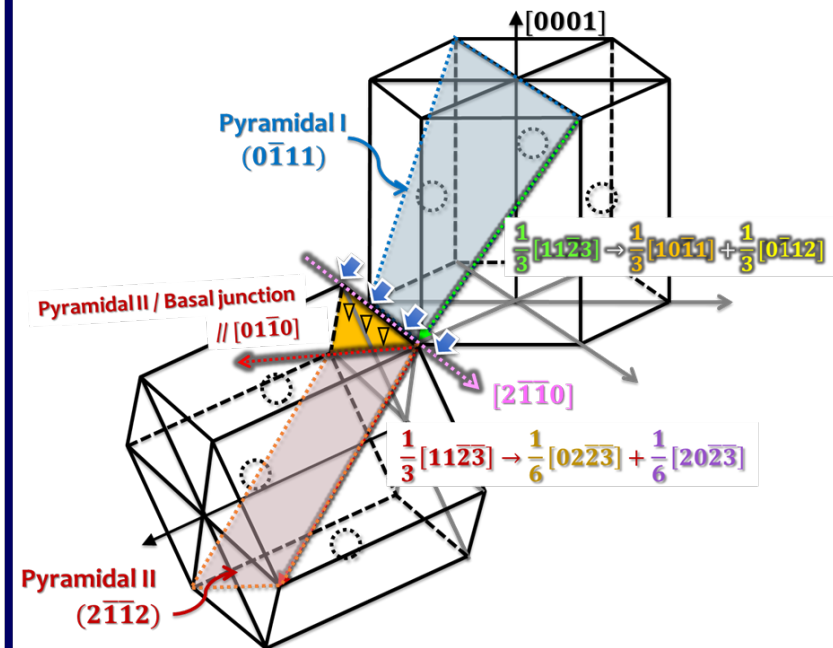


Fig. 10

	Route 0	Route I	Route II	Route III
Dissociation reaction	No dissociation			
Dislocation reaction		$\frac{1}{2}[\bar{1}01] \rightarrow \frac{1}{3}[\bar{1}\bar{1}\bar{1}] + \frac{1}{6}[\bar{1}21]$	$\frac{1}{2}[\bar{1}01] \rightarrow \frac{1}{6}[\bar{1}\bar{1}2] + \frac{1}{6}[\bar{2}11]$	$\frac{1}{2}[\bar{1}01] \rightarrow \frac{1}{6}[\bar{1}21] + \frac{1}{6}[\bar{1}01] + \frac{1}{6}[\bar{1}21]$
Thompson's notation		$CA \rightarrow C\gamma + \gamma A$	$CA \rightarrow C\delta + \delta A$	$CA \rightarrow C\beta + \beta\gamma + \gamma A$

Fig. 11

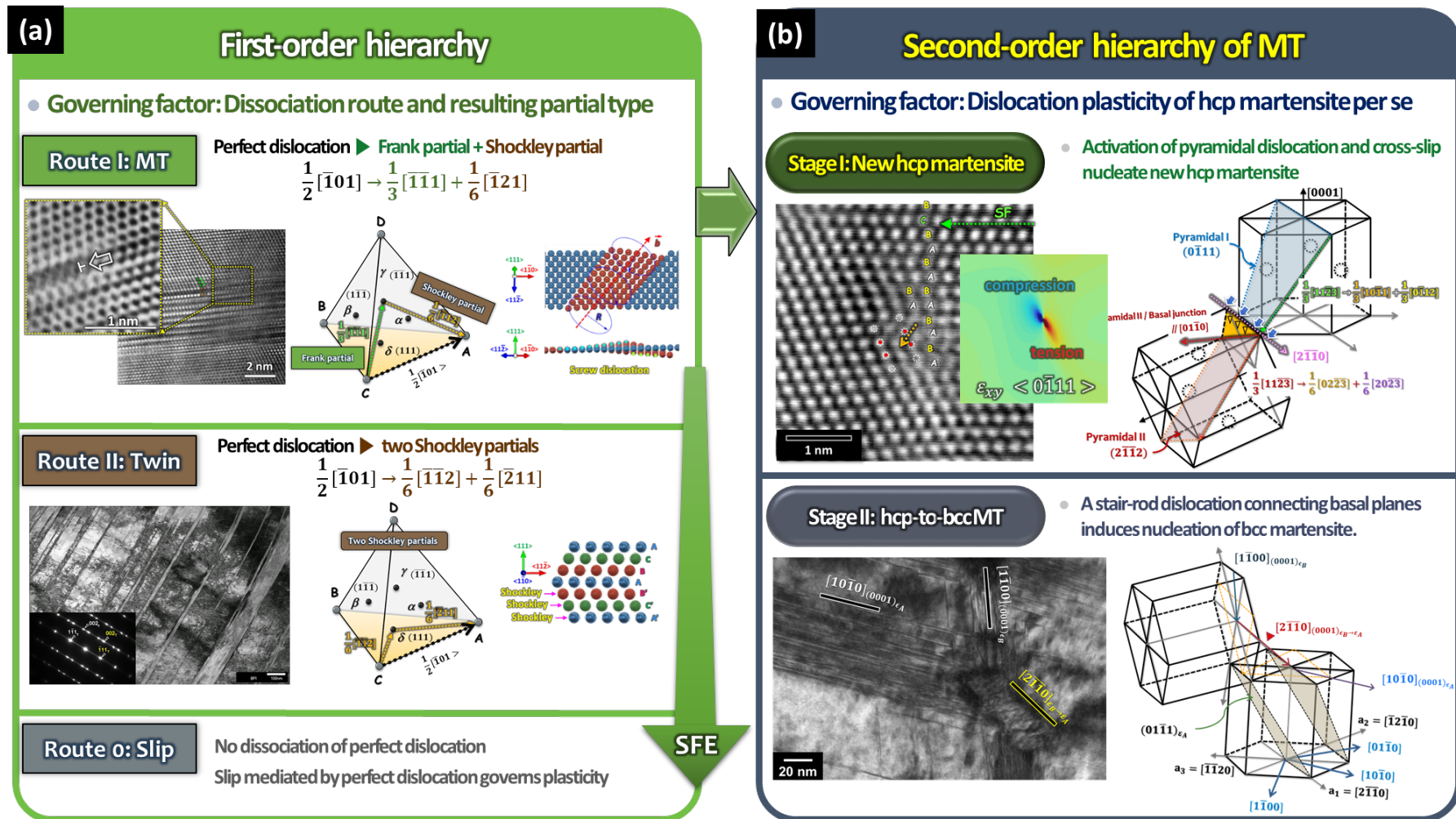


Fig. 12

Table 1. Invisibility criteria to determine Burgers vectors of dislocations ( $\vec{g}$  is the diffraction vector and  $\vec{b}$  is the Burgers vector).

 visible  invisible

	<a> perfect			<a> partial			<c+a> perfect			<c+a> partial						<c>
	$\pm \frac{1}{3} [11\bar{2}0]$	$\pm \frac{1}{3} [\bar{1}2\bar{1}0]$	$\pm \frac{1}{3} [\bar{2}110]$	$\pm \frac{1}{3} [\bar{1}100]$	$\pm \frac{1}{3} [10\bar{1}0]$	$\pm \frac{1}{3} [01\bar{1}0]$	$\pm \frac{1}{3} [11\bar{2}\bar{3}]$	$\pm \frac{1}{3} [\bar{1}21\bar{3}]$	$\pm \frac{1}{3} [\bar{2}11\bar{3}]$	$\pm \frac{1}{6} [20\bar{2}\bar{3}]$	$\pm \frac{1}{6} [02\bar{2}\bar{3}]$	$\pm \frac{1}{6} [\bar{2}20\bar{3}]$	$\pm \frac{1}{3} [10\bar{1}1]$	$\pm \frac{1}{3} [0\bar{1}1\bar{2}]$	$\pm \frac{1}{6} [1\bar{1}0\bar{3}]$	$\pm [0001]$
0002	0	0	0	0	0	0	$\pm 2$	$\pm 2$	$\pm 2$	$\pm 1$	$\pm 1$	$\pm 1$	$\pm \frac{2}{3}$	$\pm \frac{4}{3}$	$\pm 1$	$\pm 2$
2 $\bar{1}\bar{1}0$	$\pm 1$	$\mp 1$	$\mp 2$	$\pm 1$	$\pm 1$	0	$\pm 1$	$\mp 1$	$\mp 2$	$\pm 1$	0	$\pm 1$	$\pm 1$	0	$\pm \frac{1}{2}$	0
$\bar{1}2\bar{1}0$	$\pm 2$	$\pm 1$	$\mp 1$	$\pm 1$	0	$\pm 1$	$\pm 2$	$\pm 1$	$\mp 1$	0	$\mp 1$	$\mp 1$	0	$\pm 1$	$\pm \frac{1}{2}$	0
01 $\bar{1}1$	$\pm 1$	$\pm 1$	0	$\mp \frac{1}{3}$	$\pm \frac{1}{3}$	$\pm \frac{2}{3}$	$\pm 2$	$\pm 2$	$\pm 1$	$\pm \frac{5}{6}$	$\pm \frac{1}{6}$	$\pm \frac{1}{6}$	0	$\pm \frac{1}{3}$	$\pm \frac{1}{3}$	$\pm 1$
0 $\bar{1}12$	$\mp 1$	$\mp 1$	0	$\pm \frac{1}{3}$	$\mp \frac{1}{3}$	$\mp \frac{2}{3}$	$\mp 3$	$\mp 1$	$\mp 2$	$\mp \frac{11}{6}$	$\mp \frac{5}{6}$	$\mp \frac{7}{6}$	$\mp \frac{2}{3}$	$\pm \frac{4}{3}$	$\pm \frac{4}{3}$	$\mp 3$
0 $\bar{2}2\bar{1}$	$\mp 2$	$\mp 2$	0	$\pm \frac{2}{3}$	$\pm \frac{2}{3}$	$\pm \frac{4}{3}$	$\mp 1$	$\pm 3$	$\mp 1$	$\mp \frac{1}{6}$	$\mp \frac{5}{6}$	$\mp \frac{1}{6}$	$\mp 1$	$\pm \frac{2}{3}$	$\mp \frac{1}{6}$	$\mp 1$

Table 2. The angles between important planes and directions related to pyramidal dislocation in two zone axes ( $z = [2\bar{1}\bar{1}0]$  and  $z = [0001]$ ) calculated from stereographic projection (SP).

	Description			Angle (degree)	
$z = [0001]$	Perfect $\langle c+a \rangle$ dislocations of $\varepsilon_A$ and $\varepsilon_{New}$	$[\bar{1}2\bar{1}3]$	$[\bar{1}\bar{1}23]$	54.19	
	Pyramidal I planes of $\varepsilon_A$ and $\varepsilon_{New}$	$(0\bar{1}11)$	$(10\bar{1}1)$	99.54	
			$(1\bar{1}01)$	52.31	
			$(01\bar{1}1)$	123.67	
	Perfect and partial $\langle c+a \rangle$	$[\bar{1}2\bar{1}3]$	$[\bar{1}\bar{1}01]$	24.02	
			$[01\bar{1}2]$	15.24	
	Two partial $\langle c+a \rangle$	$[\bar{1}101]$	$[01\bar{1}2]$	39.27	
	$\langle c+a \rangle$ & basal-pyramidal I intersection (cross slip node)	$[\bar{1}2\bar{1}3]$	$[2\bar{1}\bar{1}0]$	105.24	
			$[\bar{1}2\bar{1}0]$	58.27	
			$[\bar{2}110]$	74.76	
$z = [2\bar{1}\bar{1}0]$	$\langle c+a \rangle$ & basal-pyramidal I intersection (cross slip node)	$[11\bar{2}3]$	$[1\bar{2}10]$	105.24	
			$[11\bar{2}0]$	58.27	
			$[2\bar{1}\bar{1}0]$	74.76	
	$\langle c+a \rangle$ & basal-pyramidal II intersection (cross slip node)	$[01\bar{1}0]$	$[11\bar{2}3]$	62.91	
			$[1\bar{2}13]$	117.09	
			$[2\bar{1}\bar{1}3]$	90	